



Research papers

FracDetect: A novel algorithm for 3D fracture detection in digital fractured rocks



Hamed Lamei Ramandi^{a,*}, Saad Irtza^b, Tharmakulasingam Sirojan^b, Aous Naman^b, Reji Mathew^b, Vidhyasaharan Sethu^b, Hamid Roshan^a

^a School of Minerals and Energy Resources Engineering, UNSW Sydney, NSW 2052, Australia

^b School of Electrical Engineering and Telecommunications, UNSW Sydney, NSW 2052, Australia

ARTICLE INFO

This manuscript was handled by Jiri Simunek, Editor-in-Chief

Keywords:
Fracture detection
Micro-CT image
Computer vision
Fractured media

ABSTRACT

Fractures have a governing effect on the physical properties of fractured rocks, such as permeability. Accurate representation of 3D fractures is, therefore, required for precise analysis of digital fractured rocks. However, conventional segmentation methods fail to detect and label the fractures with aperture sizes near or below the resolution of 3D micro-computed tomographic (micro-CT) images, which are visible in the greyscale images, and where greyscale intensity convolution between different phases exists. In addition, conventional methods are highly subjective to user interpretation. Herein, a novel algorithm for the automatic detection of fractures from greyscale 3D micro-CT images is proposed. The algorithm involves a low-level early vision stage, which identifies potential fractures, followed by a high-level interpretative stage, which enforces planar continuity to reject false positives and more reliably extract planar fractures from digital rock images. A manually segmented fractured shale sample was used as the groundtruth, with which the efficacy of the algorithm in 3D fracture detection was validated. Following this, the proposed and conventional methods were applied to detect fractures in digital fractured coal and shale samples. Based on these analyses, the impact of fracture detection accuracy on the analysis of fractured rocks' physical properties was inferred.

1. Introduction

Fracture networks in rocks are generally complex. They can range from micro-scale fractures in rock cores of a few cubic millimetres to mega-scale fractures and faults of a few thousand kilometres in the earth crust. Accurate characterisation of the fracture network is important in many disciplines, such as water, petroleum, mining and civil engineering. Fractures, particularly conductive fractures, can greatly impact the physical properties of any rocktype. In terms of fluid flow, well-connected fractures enhance the permeability of the rocks significantly, especially for tight rocktypes.

A range of techniques have been developed to characterise and visualise fracture networks at core-scale, such as optical microscopy (Serati et al., 2021; Zhang et al., 1999), scanning electron microscopy (SEM) (Fonseka et al., 1985; Lindqvist et al., 1984; Ramandi et al., 2016a; Zhou et al., 2016), neutron tomography (Christe et al., 2007; Siddiqui et al., 2021) and X-ray micro-computed tomography (micro-

CT) (Arshadi et al., 2017; Gomila et al., 2021; Lv et al., 2019; Qi et al., 2018; Ramandi et al., 2015; Ramandi et al., 2017; Roshan et al., 2019).

Permeability of the fractured rocks with low matrix permeability is primarily controlled by dimensions, spacing, connectivity, and mineralisation level of the fractures (Ramandi et al., 2016b; Zhao et al., 2021). Measuring aperture attributes locally and taking into account their variations are highly complex tasks. Therefore, for fluid flow analysis, fractures have traditionally been simplified as a set of parallel plates, and the cubic law is applied to simulate the flow (Al-Raoush and Papadopoulos, 2010; Karpyn et al., 2007). However, it is now well established that the fractures are rough-walled channels significantly influencing the flow regimes (Al-Raoush and Papadopoulos, 2010; Li et al., 2020; Pruess and Tsang, 1990; Wang et al., 2021).

Among different imaging techniques, the micro-CT technique possesses the advantage of the provision of high-fidelity high-resolution non-destructive 3D images suitable for numerical simulations. The technique can capture geometrically complex natural fractures.

* Corresponding author at: School of Minerals and Energy Resources Engineering, UNSW Sydney, NSW 2052, Australia.

E-mail addresses: h.lameiramandi@unsw.edu.au (H.L. Ramandi), t.sirojan@unsw.edu.au (T. Sirojan), aous@unsw.edu.au (A. Naman), reji.mathew@unsw.edu.au (R. Mathew), v.sethu@unsw.edu.au (V. Sethu), h.roshan@unsw.edu.au (H. Roshan).

However, to characterise the fractured rock attributes quantitatively, the greyscale multiphase micro-CT images need to be segmented into different unique phases that are homogeneous with respect to some characteristic. The number of labels (phases) depends on the purpose of the study and the available micro-CT image data, and its quality. For flow simulation, a two-phase digital rock where void space and solid phases are labelled is usually required. However, three-phase digital rocks, including resolved void spaces, solid-phase and sub-resolution void spaces (voxels that are partially filled with void spaces), are also used for flow simulation, which account for the influence of micro-voids on permeability (Qajar et al., 2012; Soulaine et al., 2016). Hybrid and dual-domain models, where a resolved phase (generally a high-permeability phase) and sub-resolution phase (generally a relatively low-permeability phase) are uniquely labelled, are also employed to compute the transport properties of digital porous media (Soulaine et al., 2016; Yang et al., 2019). Segmentation is, therefore, the most crucial step in image processing that will have a profound impact on all subsequent image analyses and simulations (Iassonov et al., 2009; Schlüter et al., 2014). Several free and commercial software toolboxes have been developed with some form of image processing, analysis and visualisation capabilities, such as ImageJ (Schneider et al., 2012), ITK (Ibanez et al., 2005), Blob3D (Ketcham, 2005), scikit-image (Van der Walt et al., 2014), ScanIP, Segment, 3DVIEWNIX and Amira-Avizo.

The number of segmentation methods in the literature exceeds a hundred (Iassonov et al., 2009), and a small fraction of those are specifically targeted fractured media. However, no segmentation method excels at all segmentation tasks and performs an errorless segmentation. Several classification schemes have been proposed in the literature for image segmentation, with a number of methods included in more than one class (Iassonov et al., 2009). Global thresholding methods include approaches where voxels are classified based on greyscale histogram evaluation only, without considering how the greyscale values are spatially arranged in corresponding images (Schlüter et al., 2014; Sezgin and Sankur, 2004; Stathis et al., 2008). In contrast, locally adaptive segmentation methods include those making a segmentation decision for each voxel using neighbourhood statistics. It is known that, in general, employing local information can provide relatively satisfying segmentation results (Deng et al., 2016; Schlüter et al., 2014; Stathis et al., 2008). A comprehensive survey by Schlüter et al. (2014) discussed a number of well-known segmentation methods and showed that the converging active contours (CAC) method is well suited for multiphase segmentation of micro-CT images. CAC uses local gradient and intensity (greyscale value) information at the same time (Sheppard et al., 2004). Its major drawback lies in its sensitivity to seed region detection and the adjustment of parameters for the speed function (Iassonov et al., 2009). CAC techniques also cannot extract all the fractures in the fractured 3D images (Ramandi et al., 2017; Ramandi et al., 2018). Furthermore, almost all segmentation methods need some inputs from the user, making the segmentation processes a subjective task. Different segmentation results are thus obtained from users with different levels of expertise, which makes the comparison of different data and results challenging and erroneous. Several approaches based on the deep learning technique have been recently proposed (Asadi and Beckingham, 2021; Cheng and Guo, 2017; Karimpouli et al., 2020b; Li et al., 2019; Wang et al., 2019). However, a major issue when adopting such methods is that they require large training datasets comprising of a large number of correctly segmented images, but such datasets are not widely available. Additionally, a deep learning system trained on a dataset is generally only accurate for the same specific rock sample from which the training data is obtained. Therefore, the subjectivity of segmentation remains a significant challenge.

The presence of discontinuities such as ridges, valleys and fractures in images all correspond to high levels of change of the imagery data within a confined local spatial region. For this reason, first and second

order gradient information is often used in feature detection tasks. Prior works (Eberly et al., 1994; Lopez et al., 1999) have utilised second order information, in the form of eigenvectors and eigenvalues of the Hessian matrix, along with first order local gradient calculations of the image data, to identify local maxima (ridges) and minima (valleys) in the direction of main principal curvature. Such approaches are successful in detecting curves or “skeletons” corresponding to ridges and valleys in images but are not designed to detect and segment fractures of varying width. The method proposed in this paper also employs the Hessian matrix to determine local curvature characteristics; however, this information is used to identify a volumetric region of high curvature as opposed to a curve of local maxima/minima points.

In general, eigenvalue decomposition of the Hessian matrix has been deployed for feature detection in a range of applications from medical (Fornaro et al., 2010; Frangi et al., 1998) to geoscience (Liang, 2016) imaging. Its utility arises from the fact that eigenvalues of the matrix correspond to local contrast changes along the principal directions of curvature as defined by the eigenvectors. As an extension to this approach, Voorn et al. (2013) investigated deploying the Hessian matrix at multiple scales to identify fractures in 3D images. This work is closely related to the method proposed in this study, with the multiscale approach suited to extracting fractures with a range of apertures from image datasets. Important differences between the two approaches relate to the way in which eigenvalue information is utilised to identify potential fracture regions. The proposed approach avoids the normalisation and calibration steps applied to eigenvalues at each voxel and substantially reduces the input parameters that are required for the Hessian filtering stage. As explained in later sections, the proposed approach directly compares the largest eigenvalue at each location with a contrast threshold that is determined from input image statistics and multiscale Hessian filter characteristics, thereby eliminating any need for specific user defined parameters. Furthermore, complementing the high-pass Hessian analysis, the proposed method implements a directional low-pass filtering stage to address issues caused by noise and problematic small high contrast structures that are often accentuated by high-pass Hessian filtering at the finest scale.

Currently, the orientation information provided by the eigenvectors of the Hessian matrix is not used and remains a topic of interest for future work. The orientation of the Gaussian disc is calculated independently from the Hessian matrix, allowing both processing stages to remain separate and thereby complementary to each other.

In this study, we thus present FracDetect, a novel algorithm for detecting fractures from greyscale 3D micro-CT that combines the advantages of voxel-level fracture detection similar to global thresholding methods, with the accuracy of locally adaptive segmentation methods in a two-stage framework. Specifically, in the first stage of the proposed algorithm, individual voxels in the 3D micro-CT image that could correspond to fractures are identified based on two principles: (a) along the direction perpendicular to a fracture, two sharp changes in voxel intensity can be expected corresponding to the edges of the fracture; and (b) a fracture is locally planar and has a much shorter extent along one direction compared to the other two orthogonal directions. This is followed by a second stage, which imposes the constraint that voxels corresponding to a fracture must be connected to other such voxels and cannot be isolated. The proposed algorithm is also developed with a view of minimising the number of the threshold values that will need to be manually tuned, with the most relevant thresholds in the algorithm automatically inferred from the 3D image data. The algorithm's performance is assessed by comparing its output with a manually segmented fractured shale sample. Additionally, the algorithm is employed on fractured shale and coal samples, and the results are compared with those obtained from conventional segmentation methods.

2. Material and methods

2.1. Digital rock data acquisition

A shale and a coal sample were used in this study as two cases of low permeability rocks containing fractures. The shale sample was an organic-rich shale obtained from the Middle Velkerri Formation, Bee-taloo sub-basin, the state of Northern Territory, Australia. Details on the petrophysical properties of the shale can be found in Algaazlan et al. (2019). The sample contained 3.15 wt% organic carbon and major clay minerals were illite-muscovite (15.7 wt%) and illite-smectite (7.4 wt%).

The coal sample was sub-bituminous coal from the Baralaba Coal Measures on the south-eastern flank of the Bowen Basin, the state of Queensland, Australia. Details on the coal specifications, including petrophysical properties and proximate and ultimate analyses results, are given in Ramandi et al. (2016b).

Micro-CT imaging of the samples was conducted using a helical micro-CT scanner (Sheppard et al., 2014). The helical scanner uses a double helix scanning trajectory (Varslot et al., 2012) to acquire data that facilitate efficient utilisation of the available X-ray flux (Sheppard et al., 2014). The scanner acquires a series of projections from the sample at different viewing angles. The projections characterise the cumulative attenuation of the X-ray beam through the sample. The acquired projections are then entered into a reconstruction algorithm based on Katsevich (2002) to reconstruct a 3D image (tomogram). The tomograms are usually presented in 16-bit greyscale images, where each data point characterises the effective X-ray attenuation coefficient of the sample at that specific point. More details on the helical scanner and its specifications can be found in Sheppard et al. (2014) and Ramandi et al. (2016a).

The imaged volume of the shale sample was a cylindrical core with a diameter of about 13 mm and a length of about 20 mm, with a resolution of $\sim 13.6 \mu\text{m}$. The coal image had a diameter of about 25 mm and a length of about 35 mm, with a resolution of about $\sim 16.5 \mu\text{m}$.

2.2. Proposed algorithm

A novel two-stage algorithm, which includes a low-level early vision stage and a high-level interpretative stage, is proposed for fracture detection. The low-level stage, which is referred to as a fracture map here, generates an initial estimate of whether a fracture exists at each location in the 3D digital rock. Following this, the high-level stage imposes reasonable constraints that fractures are not small, isolated regions. For the low-level stage, two separate filtering steps that complement each other are used. One employs the Hessian matrix, while the other utilises an oriented Gaussian disc. A block diagram of the proposed algorithm is shown in Fig. 1. The Hessian matrix provides high-pass frequency information pertaining to rapid changes in image

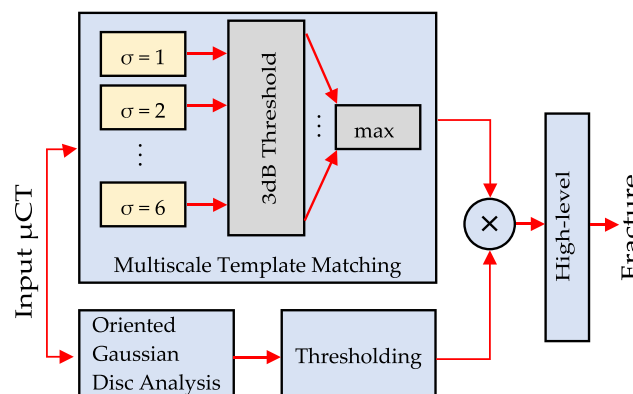


Fig. 1. A block diagram of the proposed algorithm.

data. While this stage is important to detecting fractures, the presence of noise and small isolated structures can be problematic, especially at the finer scales of the multiscale approach. To address these issues, a complementary oriented Gaussian filtering stage is also implemented, providing adaptive low-pass information that is used with a conservative threshold to reduce falsely detected fracture regions from the high-pass Hessian filtering stage. To remain sensitive to small structures, such as high-intensity blobs in the image data, the standard deviation of the oriented Gaussian disc filter is chosen to be 1 in all test cases. The applied diameter of the disc filter is also chosen to be small (refer to Table 1) to match the local planar geometry of fractures.

To provide more insight into the operation of each stage and to highlight the complementary nature of the two filtering steps, Fig. 2 is presented to show the output of each processing stage for two different input image samples. In Fig. 2(a), a potential problematic region in the input slice, comprised of white blobs with sharp edges, is highlighted (red dashed line rectangle). The corresponding output of each of the two filtering stages is shown by the accompanying binary images on the top row, where black corresponds to potential fracture regions, and white refers to the absence of any fracture features. The multiscale Hessian filter incorrectly classifies parts of the problematic region as potential fractures (e.g. edges of the white blobs), while the oriented Gaussian filter is able to correctly discard these regions. In the alternative example in Fig. 2(d), the problematic region is caused by a slow varying grey area (red dashed line oval). While this region is correctly classified by the multiscale Hessian filter, it is falsely identified as a fracture by the oriented Gaussian filter. In both cases, combining the output of the two filtering stages produces a more reliable and faithful segmentation result. The final segmented output produced by the proposed algorithm, along with corresponding groundtruth for the two input samples, are shown in Fig. 3. The segmented results in the top and bottom rows of Fig. 3 correspond to the respective input samples shown in the top and bottom rows of Fig. 2.

2.2.1. The Hessian matrix for fracture detection

In the proposed method, the second derivative of Gaussian, shown in Fig. 4, serves as a template for fracture matching. In typical greyscale tomograms, low X-ray attenuating materials, e.g. air, are presented by low greyscale values. As such, an empty fracture, which is filled with the air, appears darker than its adjacent regions in the tomograms. Filtering with the template thus produces positive responses in locations where fractures exist locally. The “width” of the template can be adjusted by modifying the standard deviation, σ , of the Gaussian. In this work, a set of standard deviations, σ , is employed to accommodate a range of possible fracture widths.

Template matching can be efficiently implemented as a convolution with a mirror image of the template, but since the second derivative is symmetric, mirroring is redundant. Here the 3D digital rock is denoted as $V(\mathbf{s})$, where $\mathbf{s}^T = (s_x, s_y, s_z)$ is a location within that image. Then,

$$V_{xx}^\sigma(\mathbf{s}) = \left(\frac{\partial^2 G^\sigma}{\partial s_x^2} * V \right)(\mathbf{s}) = \left(G^\sigma * \frac{\partial^2 V}{\partial s_x^2} \right)(\mathbf{s}) = \frac{\partial^2}{\partial s_x^2} (V * G^\sigma)(\mathbf{s}) \quad (1)$$

where $G^\sigma(\mathbf{s}) = \exp(-\mathbf{s}^T \mathbf{s} / 2\sigma^2) / (2\pi\sigma^2)^{3/2}$ is the Gaussian function and $*$ is the convolution operator. Consequently, one can think of the convolution with the second derivative as being equivalent to first convolving

Table 1
User defined parameters and respective values used for each image class.

Parameters	Image Class	
	Coal	Shale
Oriented filter threshold ratio	0.7	0.9
Oriented Gaussian disc diameter	5	10

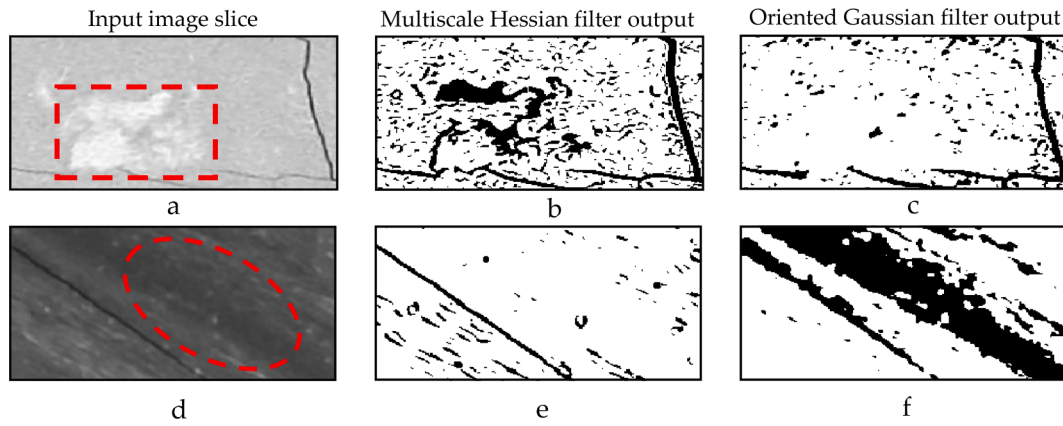


Fig. 2. Top and bottom row each shows an input image example with corresponding output of the two filtering stages. (a) and (d) show a slice of an input image with problematic regions highlighted by red dashed line rectangle/oval. Output of the multiscale Hessian filtering stage is shown in (b) and (e), while (c) and (f) show the corresponding output of the oriented Gaussian filtering stage.

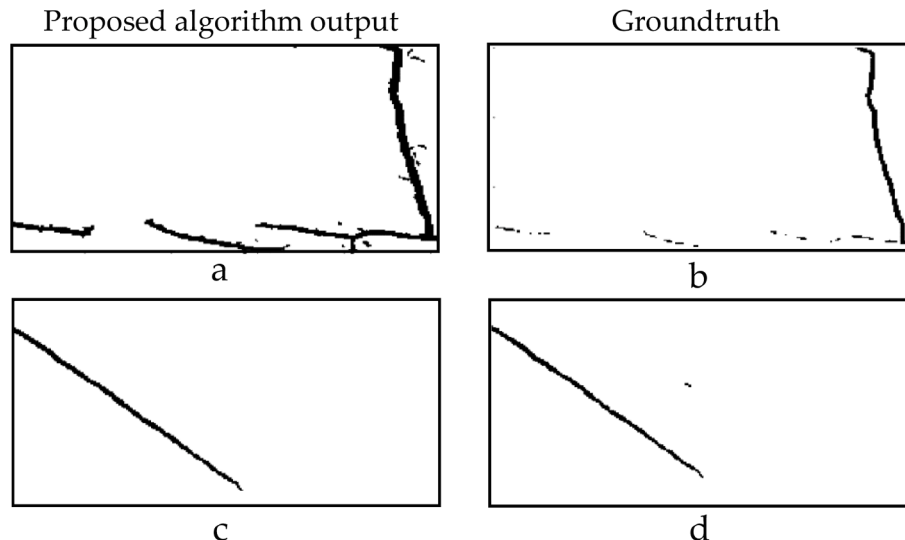


Fig. 3. Final segmented output of the proposed algorithm (left column) with corresponding groundtruth (right column) for the two input samples.

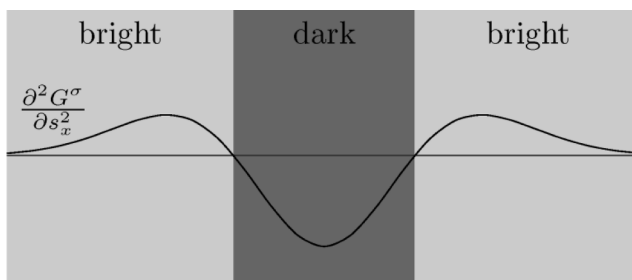


Fig. 4. A depiction of a fracture, with the second derivative of Gaussian superimposed on it, the derivative is negative in dark regions and positive in bright regions.

the rock image V with a Gaussian G^σ and then taking the second derivative. Noting that the second derivative is very sensitive to noise, this convolution with a Gaussian reduces the noise in the digital rock V and makes the result reliable.

Since fractures can occur in any orientation, it is useful to evaluate the second derivative in any direction, denoted by the direction vector \mathbf{d} , with $\|\mathbf{d}\|_2 = 1$. This can be achieved by utilising $\mathbf{d}^T \mathbf{H}^\sigma \mathbf{d}$, where \mathbf{H}^σ is the Hessian matrix of the rock image V , which is given by:

$$\mathbf{H}^\sigma(\mathbf{s}) = \begin{bmatrix} V_{xx}^\sigma(\mathbf{s}) & V_{yx}^\sigma(\mathbf{s}) & V_{zx}^\sigma(\mathbf{s}) \\ V_{xy}^\sigma(\mathbf{s}) & V_{yy}^\sigma(\mathbf{s}) & V_{zy}^\sigma(\mathbf{s}) \\ V_{xz}^\sigma(\mathbf{s}) & V_{yz}^\sigma(\mathbf{s}) & V_{zz}^\sigma(\mathbf{s}) \end{bmatrix}, \mathbf{s} \in \mathbb{R}^3 \quad (2)$$

where, the elements of the Hessian are given by second order partial derivatives of the 3D rock image, i.e., $V_{xy}^\sigma(\mathbf{s}) = \left(\frac{\partial^2 G^\sigma}{\partial s_x \partial s_y} * V \right)(\mathbf{s})$. In practice, however, acquiring the digital rock involves sampling the 3D image, $V(\mathbf{s})$, to obtain a discrete image, $V[\mathbf{n}]$, where $\mathbf{n} \in \mathbb{Z}^3$. Consequently, the second derivative of Gaussian $V_{xy}^\sigma[\mathbf{n}]$, obtained from $\left(V * \frac{\partial^2 G^\sigma}{\partial s_x \partial s_y} \right)[\mathbf{n}]$, is valid so long as the Nyquist sampling theorem is observed (σ must be around 1 or larger so that Nyquist theorem is observed for the Gaussian as well). For the discrete-domain oriented second derivative of Gaussian,

it is also well-established that it can be obtained as a linear combination of a set of 6 “basis” discrete-domain second derivatives, which are, in this work, the 6 unique partial derivatives in the Hessian matrix (Derpanis and Gryn, 2005; Freeman and Adelson, 1991). This is only valid for the second derivative of Gaussian.

Since the Hessian matrix is symmetric, it has only real eigenvalues and its eigenvectors are orthogonal. The largest magnitude eigenvalue λ_{\max}^σ is equal to the largest magnitude second derivative, and the normalised eigenvector associated with λ_{\max}^σ is the direction \mathbf{d}_{\max}^σ at which this derivative is obtained; this can be obtained from the eigenvalue definition $\mathbf{H}^\sigma \mathbf{d}_{\max}^\sigma = \lambda_{\max}^\sigma \mathbf{d}_{\max}^\sigma$; multiplying by $(\mathbf{d}_{\max}^\sigma)^T$, which lead to:

$$(\mathbf{d}_{\max}^\sigma)^T \mathbf{H}^\sigma \mathbf{d}_{\max}^\sigma = (\mathbf{d}_{\max}^\sigma)^T \lambda_{\max}^\sigma \mathbf{d}_{\max}^\sigma = \lambda_{\max}^\sigma \quad (3)$$

Normalising or scaling the eigenvector has no effect on the eigenvalue λ_{\max}^σ , since $c\mathbf{H}^\sigma \mathbf{d}_{\max}^\sigma = c\lambda_{\max}^\sigma \mathbf{d}_{\max}^\sigma$ where c is a scaling factor; also, the sign of eigenvalues does not change when the scaling factor c is negative. Negative eigenvalues are of no interest since they are associated with “anti-template,” where the rock image has a bright region between two darker regions. In the vicinity of a fracture, it is expected the direction \mathbf{d}_{\max}^σ to be perpendicular to the fracture plane, and the two eigenvalues other than the largest λ_{\max}^σ to be significantly smaller than λ_{\max}^σ .

A set Σ of standard deviations, σ , is employed in this work, where $\Sigma = \{1, 2, \dots, 6\}$; larger standard deviations can be employed for wider fractures. Then, for each standard deviation, σ , a binary image A^σ is evaluated using:

$$A^\sigma[\mathbf{n}] = \begin{cases} 1 & \lambda_{\max}^\sigma[\mathbf{n}] > \tau_A^\sigma \\ 0 & \text{otherwise} \end{cases} \quad (4)$$

where τ_A^σ is a threshold. To evaluate this threshold, a contrast value ρ is found from the difference between the mean of the digital rock $V[\mathbf{n}]$ and the mean of the smallest 3 % values in $V[\mathbf{n}]$. Then, the threshold τ_A^σ is set equal to $\rho \cdot v_{3db}$, where v_{3db} is chosen such that the width of the fracture is the distance from the point at which the response to the second derivative of Gaussian filter is half its peak to the corresponding point on the other side of the centre of the fracture. Specifically, fractures are detected by comparing regions of the rock image to the second derivative of Gaussian template, and the response to this filter would attain a local peak when the template is centred on the fracture. Here edges are defined as the points on either side where the response is 3 dB below the peak. This way, the threshold adapts to the rock image $V[\mathbf{n}]$. The generated binary image A^σ represents locations that are likely to have a fracture. Finally, the second derivative of Gaussian analysis produces:

$$A[\mathbf{n}] = \max_{\sigma \in \Sigma} A^\sigma[\mathbf{n}] \quad (5)$$

2.2.2. Oriented Gaussian disc

As noted, fracture regions correspond to lower image intensity/greyscale values, i.e., darker regions, than their neighbours. A local averaging filter is therefore applied, and this local average is compared to a global threshold determined from the statistics of the input sample; thus, no user-supplied information is required. The idea here is to evaluate the average over an oriented Gaussian disc, noting that the desired minimum filter response will always be observed when the orientation of the Gaussian disc aligns with that of the fracture. As the orientation of the fracture is unknown, one approach is to apply incrementally rotated versions of Gaussian disc and choose the minimum filter response as the one that best aligns with the fracture orientation. Such an approach is computationally expensive. A more efficient implementation can be achieved by performing operations in the Fourier domain, as explained next.

First, the rock image $V(\mathbf{s})$ is multiplied by a Gaussian function

$G_t^\sigma(\mathbf{s}) = G^\sigma(\mathbf{s} - \mathbf{t})$, centred at location \mathbf{t} , to obtain a ball

$$F_t^\sigma(\mathbf{s}) = V(\mathbf{s}) \cdot G_t^\sigma(\mathbf{s}) \quad (6)$$

In this system, Gaussian functions with a standard deviation of one are taken only; therefore, the superscript σ is dropped from all terms in this section for ease of reading. By taking the Fourier transform $\widehat{F}(\omega)$ of that ball, the Fourier transform of a series of discs $D_{t,yz}(s_x)$ perpendicular to the x -axis can be written as

$$\widehat{F}_t(\omega_x, 0, 0) = \int_{-\infty}^{\infty} \left(\underbrace{\int_{-\infty}^{\infty} \int_{-\infty}^{\infty} F_t(s) ds_y ds_z}_{D_{t,yz}(s_x)} \right) e^{-j\omega_x s_x} ds_x \quad (7)$$

The desired oriented Gaussian disc in the yz -plane at location $t_x = 0$ is then obtained using the inverse Fourier transform of $\widehat{F}_t(\omega_x, 0, 0)$; i.e.,

$$D_{t,yz}(0) = \frac{1}{2\pi} \int_{-\infty}^{\infty} \widehat{F}_t(\omega_x, 0, 0) d\omega_x \quad (8)$$

Discs in other orientations can similarly be obtained by integrating the Fourier transformed function $\widehat{F}(\omega)$ in a direction perpendicular to the plane of the disc. In this work, experimental results have shown that it is sufficient to evaluate only three such discs $D_{xy}[\mathbf{n}]$, $D_{yz}[\mathbf{n}]$, and $D_{xz}[\mathbf{n}]$. The minimum of this disc $D_{\min}[\mathbf{n}] = \min\{D_{xy}[\mathbf{n}], D_{yz}[\mathbf{n}], D_{xz}[\mathbf{n}]\}$ is then computed as this would correspond to the most likely orientation of the fracture that might exist at that location.

Similar to Section 0, binary image $B[\mathbf{n}]$ is evaluated using

$$B[\mathbf{n}] = \begin{cases} 1 & D_{\min}[\mathbf{n}] < \tau_B \\ 0 & \text{otherwise} \end{cases} \quad (9)$$

where τ_B is a threshold obtained from

$$\tau_B = \frac{\beta}{|\mathbf{n}|} \sum_{\mathbf{n}} \min\{D_{\min}[\mathbf{n}], \mu_V\} \quad (10)$$

where $|\mathbf{n}|$ is the number of voxels in the digital rock $V[\mathbf{n}]$, μ_V is the mean of $V[\mathbf{n}]$ and β is a user defined ratio typically in the range of 0.7 to 0.9. A final candidate fracture map $C[\mathbf{n}]$ is obtained using $A[\mathbf{n}] \cdot B[\mathbf{n}]$.

2.2.3. High-level interpretation

The Hessian and oriented Gaussian filtering stages provide local, low-level features summarised in the form of a binary map. It is important to note that both filtering stages remain agnostic to any high-level information such as expected fracture length and volume. The high-level analysis stage shown in Fig. 1 considers the individual binary voxels over a wide spatial span and measures attributes of connected components such as major axis length and volume. These measured attributes are then compared to expected values to decide if observed connected components are representative of fractures.

The high-level analysis is performed on the candidate fracture map $C[\mathbf{n}]$. Fracture regions, as noted before, are typically not small, isolated regions but form part of a larger spatially connected set of voxels in disc form. 3D connectivity analysis (He et al., 2017; Toriwaki and Yoshida, 2009) is therefore employed to remove small connected regions potentially caused by noise while retaining 3D regions that exceed certain minimum limits. More specifically, connectivity analysis is performed on the binary candidate fracture map $C[\mathbf{n}]$, identifying sets S_i comprised of maximal spatially connected candidate voxels. A 6-neighbour 3D connectivity criteria is used such that voxels at locations \mathbf{n}_1 and \mathbf{n}_2 are considered to be directly connected if $C[\mathbf{n}_1] = C[\mathbf{n}_2] = 1$ and $\|\mathbf{n}_2 - \mathbf{n}_1\|_2 = 1$. The two attributes of major axis length and volume of a connected component S_i can be best described in terms of its corresponding raw moments $M_{pqr}^{(i)}$ and normalised central moments $\mu_{pqr}^{(i)}$

(Gonzalez and Woods, 2018) as defined below;

$$M_{pqr}^{(i)} = \sum_{\mathbf{n} \in S_i} n_x^p \cdot n_y^q \cdot n_z^r \quad (11)$$

$$\mu_{pqr}^{(i)} = \frac{1}{M_{000}^{(i)}} \sum_{\mathbf{n} \in S_i} (n_x - \bar{n}_x)^p \cdot (n_y - \bar{n}_y)^q \cdot (n_z - \bar{n}_z)^r \quad (12)$$

where $\mathbf{n} = [n_x, n_y, n_z]$ and $(\bar{n}_x, \bar{n}_y, \bar{n}_z) = \left(\frac{M_{100}^{(i)}}{M_{000}^{(i)}}, \frac{M_{010}^{(i)}}{M_{000}^{(i)}}, \frac{M_{001}^{(i)}}{M_{000}^{(i)}} \right)$ refers to the centroid of the region S_i . To determine the major axis length attribute, $l^{(i)}$, an ellipsoid centred at $(\bar{n}_x, \bar{n}_y, \bar{n}_z)$ is constructed such that the spatial region E_i bounded by the ellipsoid corresponds to the same second order normalised central moments as S_i (Chaumette, 2004; Rocha et al., 2002). That is, moments $\mu_{pqr}^{(i)}$ for $p+q+r=2$ remain the same when Eq. (11) and (12) are redefined for $\mathbf{n} \in E_i$. The major axis length $l^{(i)}$ is the largest diameter of this constructed ellipsoid modelling S_i . In this work, $l^{(i)}$ is compared to a threshold L and if $l^{(i)} < L$ then the corresponding set is eliminated as a potential fracture candidate. The volume attribute $v^{(i)} = M_{000}^{(i)}$ is essentially the number of voxels comprising S_i and is similarly compared to a corresponding threshold value Y . If $v^{(i)} < Y$ then S_i is omitted as a candidate.

The lower limit threshold values of L and Y are based on observations of collections of both Coal and Shale samples with available groundtruth data, and remain fixed for all test cases considered in this study. The value for L is derived as a fixed ratio λ of the minimum dimension of the input rock sample, such that

$$L = \lambda \cdot \min \{ \dim_x, \dim_y, \dim_z \} \quad (13)$$

where \dim_x, \dim_y, \dim_z represent the width, height and depth of the test sample. The volume threshold Y is derived from average lower limits observed from groundtruth data and also remains unaltered in all experiments without any need for user input. Both L and Y are subject to imaging system parameters, including the achieved image resolution, and the scale at which fractures are required to be detected. If these parameters and requirements are consistent for the collection of rock samples being analysed then as shown by the experimental results, values for L and Y can remain unchanged.

2.2.4. User defined parameters

The proposed method recommends a certain process for determining user defined input parameters. For each class of images, input parameters are first determined on an exemplar and then fixed for all other 3D image samples belonging to the same class. For example, in Section 3, an exemplar of the shale class is used to determine the free parameters, which then remain unaltered when processing other shale test samples. Due to substantially differing image statistics between image classes (e.g. shale and coal), it is not feasible to employ a single set of input parameters across all image datasets.

A list of required user defined parameters and their respective values used in this study for each class of input images is shown in Table 1. Note that there are only two free parameters required for the proposed method, which is a considerable reduction in relation to other comparable approaches applied to similar types of 3D imagery. The oriented filter threshold ratio refers to the β parameter in Eq. (10), and the oriented Gaussian disc diameter refers to the spatial extent of the applied Gaussian filter.

2.2.5. Computational complexity

All steps of the proposed algorithm can be implemented with low computational complexity. For Section 2.2.1, the off-diagonal Gaussian

derivatives in Eq. (2), which has the form $G^\sigma(\mathbf{s}) \cdot s_x s_y / \sigma^4$, can be implemented using separable filters. The diagonal elements, which has the form $G^\sigma(\mathbf{s}) \cdot (s_x^2 - \sigma^2) / \sigma^4$, can be implemented as the difference between two separable filters; further efficiency can be achieved if some of the intermediate steps are combined. The eigenvalues of a 3x3 matrix can be found without iterations using the algorithm proposed by Smith (1961). The algorithm in Section 2.2.2 involves a simple filtering step. For these Sections, the subsequent steps of thresholding and generating candidate fracture maps are also simple operations. For Section 2.2.3, identifying region volumes within a binary 3D volume can be performed with one pass through the volume, one plane at a time; in each pass, new regions can be created if they appear or merged if they intersect. This approach has a complexity comparable to that of filtering. Once regions within the volume are identified, the largest axis can be found by evaluating the eigenvectors of a 3x3 matrix; this step can exploit the aforementioned algorithm.

3. Results and discussions

In generating all results for the proposed algorithm, the minimum limit for the major axis length attribute L is determined by setting $\lambda = 0.5$ in accordance with Eq. (13) and the minimum volume threshold is set to $Y = 1000$. These values were chosen empirically based on observation of some coal and shale samples and were then kept unchanged since the imaging setup was not altered.

Fig. 5 shows an area near a low-density porous region. Here the simple thresholding method was used, and its results were compared with the proposed algorithm. This is because, as explained before, the number of segmentation methods exceeds a hundred (Fassonov et al., 2009), and we cannot apply and compare all of the available methods. Choosing any specific segmentation method would limit the audience to those who are familiar with that specific method. However, the simple thresholding method is one of the widely used methods, and most of the readers are familiar with the way it functions. Thus, we do not compare the relative performance of the method to the range of other fracture methods in the literature. Perhaps, the method can be complementary to other fracture segmentation methods.

It is observed that by choosing a threshold value of A, which is set to capture fractures as long as the low-density regions are not included, the fracture F cannot be segmented (Fig. 5b). Choosing a higher threshold value, B, which captures the entire fractures regardless of the inclusion of low-density regions, results in capturing a large portion of low-density regions that have greyscale values similar to Fracture F (Fig. 5c). Setting thresholds, A or B, thus, results in mislabeling of the fractures and accordingly undersegmentation and oversegmentation of the fractures present in the sample. Such undersegmentation and oversegmentation significantly impact the computation of digital rock physical properties.

Apart from imaging artefacts, which can significantly impact the quality of micro-CT images (Karimpouli et al., 2020a), some of the segmentation challenges, such as the ones discussed above, arise from inherent micro-CT imaging limitations. A common challenge with micro-CT imaging is the balance between the sample size and image resolution. The samples need to be sufficiently large to represent the rock being studied. Furthermore, in highly fractured rocks, obtaining a sample that contains a representative fracture network is highly challenging. However, the larger the sample, the coarser the micro-CT resolution. Thin fractures, thus, usually occur near the resolution limit of the image. The fractures apertures in the direction normal to fractures are generally characterised by only a few voxels, making their detection and visualisation difficult (Ramandi et al., 2017).

Moreover, in micro-CT imaging, the material at each point affects the adjacent materials intensity values due to the averaging produced by the

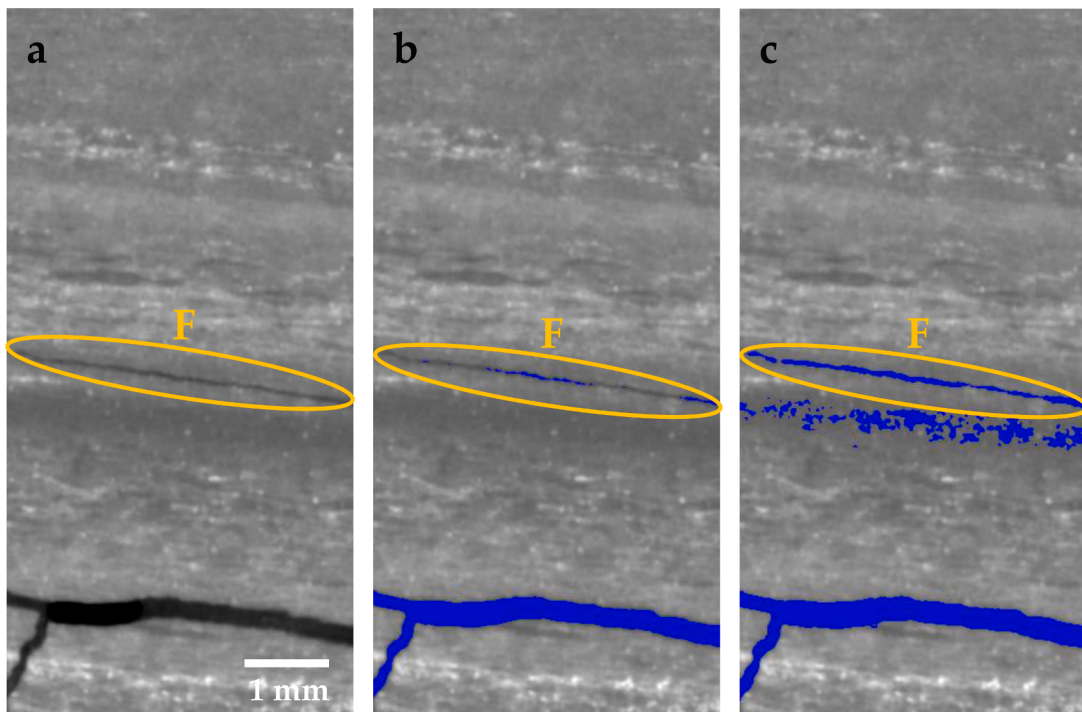


Fig. 5. A 2D section of fractures in shale occurring near (F) and above the resolution of the micro-CT image. a: the raw 2D section, b and c: areas with a greyscale value below thresholds A and B, respectively.

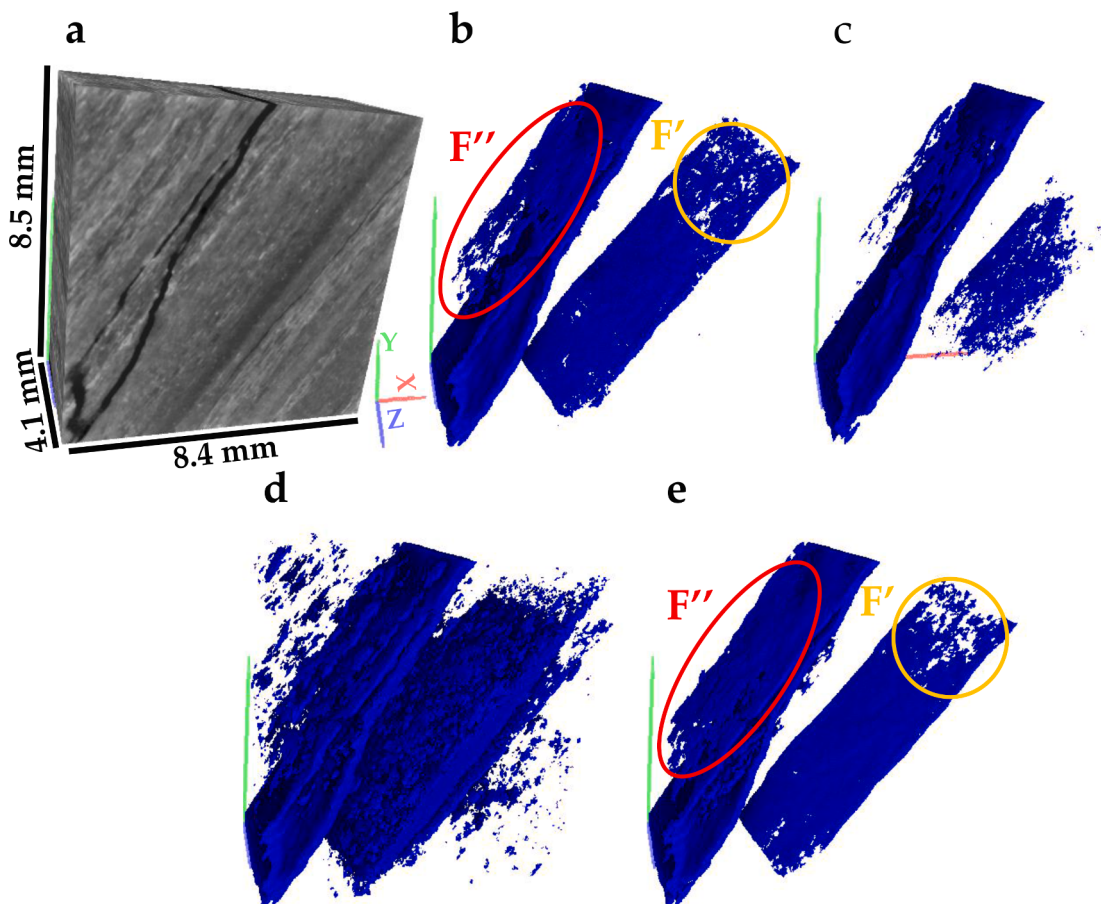


Fig. 6. a: a 3D representation of the micro-CT image of the shale sample (dark = fractures and pores, and grey and white = matrix), b: the groundtruth segmented image, c and d: the segmented images obtained by applying thresholds A and B, respectively and e: the segmented images obtained by the proposed method.

nonzero size of the X-ray focal spot and/or detectors. Therefore, the greyscale transition between two adjacent materials with different densities, such as two minerals with very high and low densities or a mineral and air (void spaces), rather than being sharp, spans several voxel widths (Ketcham, 2005). Another inherent micro-CT imaging characteristic is the partial volume effect that refers to where the volume (voxel) contains two or more materials. In such voxels, the greyscale value represents the average properties of the included materials (Hsieh, 2009; Ketcham and Carlson, 2001).

Therefore, the fractures that occur near the resolution limit of the image often obtain greyscale values between the values of void and the adjacent material. These void spaces (fractures and pores) can be segmented as a sub-resolution phase (Qajar et al., 2012; Ramandi et al., 2016b). The first step before resolving the sub-resolution phase, aperture size measurement or any other measurement is fracture detection; both the resolved and sub-resolution fractures.

Due to the above-mentioned micro-CT imaging limitations, in many digital fractured rocks, there are sub-resolution fractures that have greyscale values similar or even below that of some low density or microporous materials, which cannot be segmented using the existing methods.

To assess the proposed algorithms' performance in identifying the fractures, a portion of the shale sample (Fig. 6a) is manually segmented with caution and used as a 'groundtruth image' (Fig. 6b). The manual segmentation process, which was extremely time-consuming, included a layer by layer inspection of the image and a manual selection of the fractures. This process was facilitated by a combination of the masking and brushing tools of Avizo 9.2, as explained in Ramandi et al. (2018). Fig. 6c and d present the results of applying thresholds A and B, showing a clear undersegmentation and oversegmentation of the fractures. The result of the application of the proposed method to the digital shale sample for detection of the fractures is shown in Fig. 6e. The visual comparison of Fig. 6e with other segmentation results shows that the

proposed method achieved a more realistic fracture structure than the ones obtained by applying thresholds A and B, i.e. very similar to the groundtruth image. It is noticed that the method performs satisfactorily where the fracture apertures are near the resolution of micro-CT image, particularly in the region F'. This is because the method can connect the low greyscale values that create a fracture in any direction, which is challenging even by looking at individual voxels in some directions when the fractures are manually segmented.

The proposed method was further applied to another shale sample and two coal samples. In all images, threshold value A was set to only capture fractures without the inclusion of any other regions, while threshold B was set to capture the entire fractures, although it might include other low-density regions. Fig. 7 shows the results for the shale sample containing a couple of fractures running through higher density minerals. It is visually observed that applying thresholds A (Fig. 7b) and B (Fig. 7c) result in undersegmentation and oversegmentation, which can decrease the accuracy of the analysed data. The proposed algorithm, nevertheless, delivers relatively realistic results (Fig. 7d), as confirmed by the groundtruth image in Fig. 6. The segmentation outcomes for the coal samples are shown in Figs. 8 and 9. Similar results to that of the shale samples are seen for coal samples, where the proposed method delivers relatively realistic segmentation outcomes. In particular, the proposed method excludes the isolated islands that do not form a disc type geometry.

The only segmentation outcomes in which the fracture aperture sizes are more accurate than others are the undersegmented data (threshold A). This is because in the undersegmented data, mainly the resolved fractures, which have aperture sizes at or above the resolution limit of the image, are segmented as fractures. Fracture aperture sizes in all other images, even the groundtruth image, are inaccurate as they also contain sub-resolution fractures. This means that at least one voxel, e.g. $\sim 13.6 \mu\text{m}$ in the shale sample, is allocated to the fracture aperture even where the aperture sizes are less than the image resolution (voxel size in

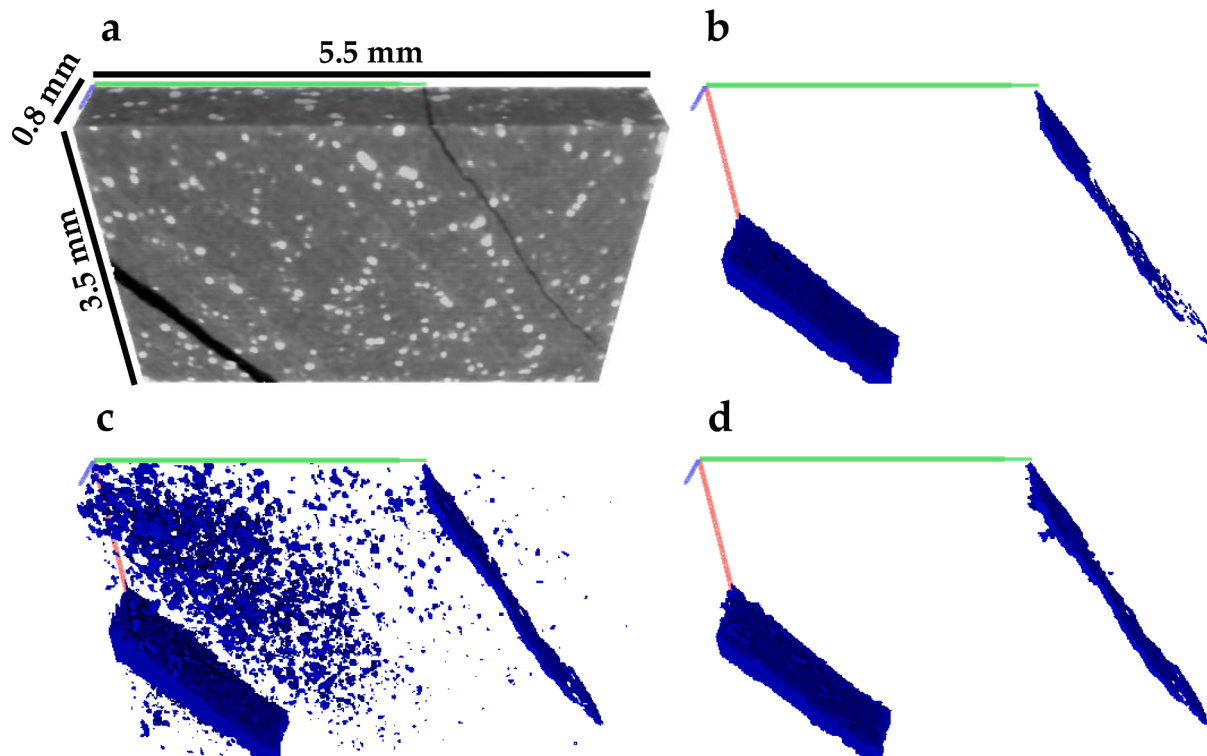


Fig. 7. a: a 3D representation of the micro-CT image of the shale sample (dark = fractures and pores, and grey and white = matrix), b and c: the segmented images obtained by applying thresholds A and B, respectively and d: the segmented images obtained by the proposed method.

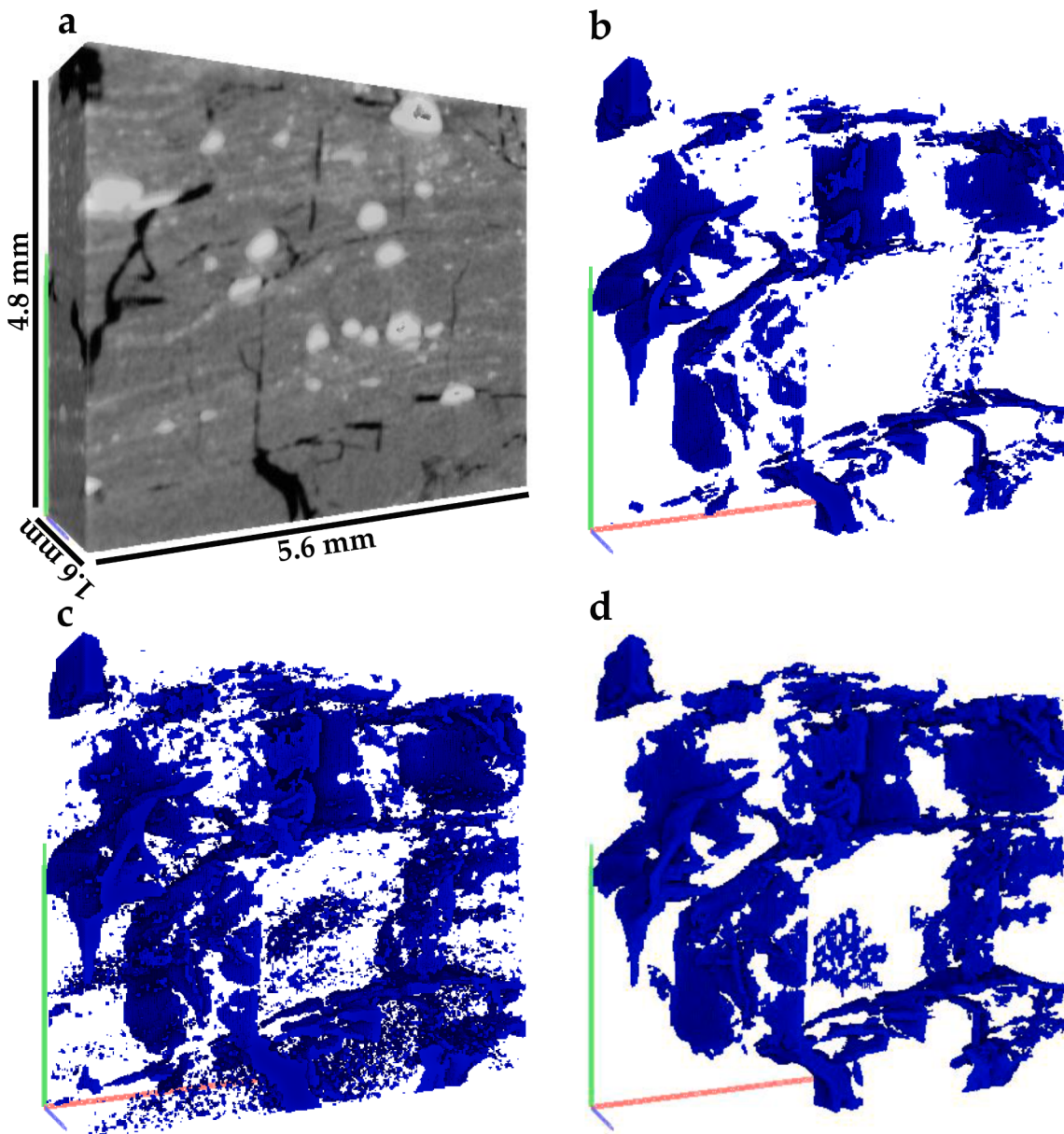


Fig. 8. a: a 3D representation of the micro-CT image of the coal sample (dark = fractures and pores, and grey and white = matrix), b and c: the segmented images obtained by applying thresholds A and B, respectively and d: the segmented images obtained by the proposed method.

this study), which is inaccurate. A few methods for fracture aperture size measurement and calibration have been developed (Johns et al., 1993; Keller, 1998; Ketcham et al., 2010; Mazumder et al., 2006; Ramandi et al., 2016a; Ramandi et al., 2017; Robert et al., 1993; Van Geet et al., 2001; Vandersteen et al., 2003; Verhelst et al., 1995), which are not within the scope of this study. However, integration of an aperture size computation method to the currently proposed algorithm is an objective for future works as the method can readily adopt fracture aperture as an input for further tuning. Producing a 3D image with accurate fracture structures and dimensions and other pore spaces would be significant for many digital rock analyses, such as petrophysical and geomechanical analyses. Here, to further analyse the impacts of the segmentation on the physical structure of the fractured samples, a skeleton of the fracture network is obtained for each image, which eliminates the impact of fracture aperture size, as presented in Fig. 10. The surface area of the

one-voxel width fractures are measured, and the surface area to volume ratio (SA:V) is then computed (Fig. 10).

Table 2 provides the SA:V results of all samples, which indicates the significant impact that the segmentation has on obtaining the fracture network and consequently computation of the physical fractured rocks properties. For the shale sample shown in Fig. 6, the SA:V results of the application of thresholds A ($4.7\text{E-}02 \text{ mm}^{-1}$) and B ($2.4\text{E-}01 \text{ mm}^{-1}$) are highly different from the groundtruth image ($7.6\text{E-}02 \text{ mm}^{-1}$), while the result of the proposed method ($8.6\text{E-}02 \text{ mm}^{-1}$) is very similar to the groundtruth. This implies that the proposed method significantly outperforms the conventional segmentation methods in terms of fracture detection. Being automatic also means that the subjectivity of the segmentation task is eliminated. This ability allows for an accurate comparison of different digital rocks as the user effect/bias is minimised.

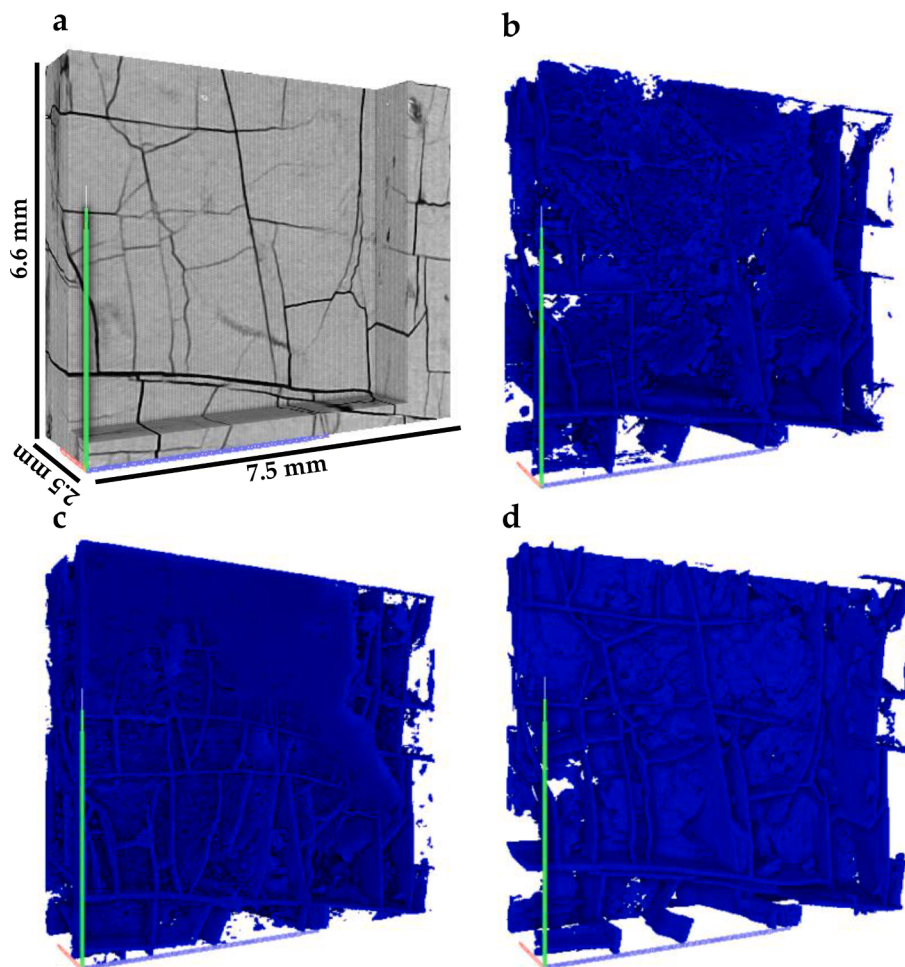


Fig. 9. a: a 3D representation of the micro-CT image of the coal sample (dark = fractures and pores, and grey and white = matrix), b and c: the segmented images obtained by applying thresholds A and B, respectively and d: the segmented images obtained by the proposed method.

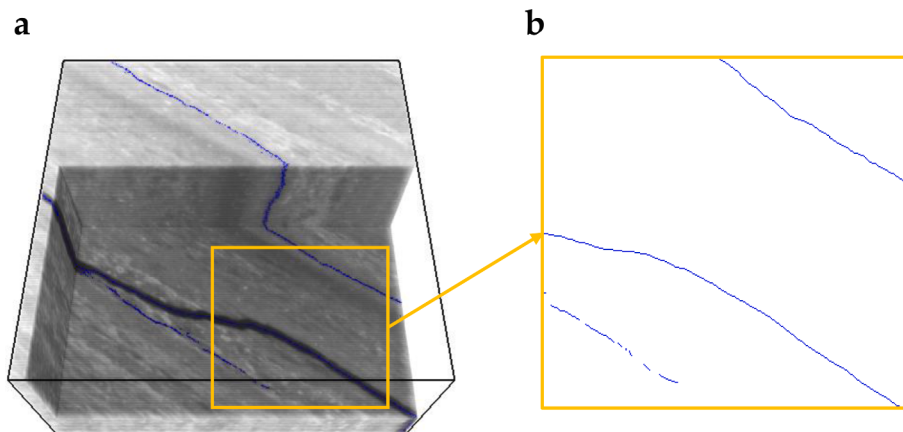


Fig. 10. a: a 3D representation of the skeleton in the shale image, and b: an enlarged portion of the highlighted.

Table 2

Surface area to volume ratio of the sample in mm^{-1} .

	Shale A	Shale B	Coal A	Coal B
Threshold A	4.7E-02	1.4E-04	2.8E-02	6.7E-03
Threshold B	2.4E-01	4.1E-04	4.7E-02	1.4E-02
Algorithm	8.6E-02	2.1E-04	3.3E-02	1.2E-02

4. Conclusion

Fractures are complex 3D features in rocks occurring at different scales. Micro-CT imaging is a reliable technique for non-destructive visualisation of fractures in core-scale rock samples. However, to accurately characterise fracture captured in micro-CT images, the greyscale images need to be segmented. Consequently, segmentation of 3D fractures in micro-CT images is a critical task for digital rock physics

analysis. The first step in fractured rocks segmentation is the detection of 3D fractures prior to determining the exact aperture sizes. The method proposed in this study is shown to be robust for detecting the 3D fractures in greyscale micro-CT images. While conventional methods generally deliver undersegmented or oversegmented results, the proposed algorithm results in appropriately segmented data, as verified by comparing with manually segmented groundtruth data. The impact of accurate detection of fractures on preserving fractures' physical properties is highlighted by computing and comparing the surface areas of skeletons of the images labelled by the proposed algorithm and conventional methods. Future work will aim to integrate an aperture measurement method with the proposed algorithm to identify realistic fracture representation.

CRediT authorship contribution statement

Hamed Lamei Ramandi: Conceptualization, Methodology, Formal analysis, Investigation, Visualization, Validation, Writing – original draft, Writing – review & editing, Project administration. **Saad Irtza:** Investigation, Visualization, Writing – original draft. **Tharmakulasingam Sirojan:** Investigation, Writing – review & editing. **Aous Naman:** Methodology, Resources, Writing – review & editing, Supervision. **Reji Mathew:** Methodology, Resources, Writing – review & editing, Supervision. **Vidhyasaharan Sethu:** Resources, Funding acquisition, Methodology, Resources, Writing – review & editing, Supervision, Project administration. **Hamid Roshan:** Resources, Funding acquisition, Conceptualization, Methodology, Resources, Writing – review & editing, Supervision, Project administration.

Declaration of Competing Interest

The authors declare that they have no known competing financial interests or personal relationships that could have appeared to influence the work reported in this paper.

Acknowledgment

The authors would like to acknowledge the financial support from UNSW Collaborative Fund and the Australian Research Council (ARC) Discovery Project 200102517.

References

- Al-Raoush, R., Papadopoulos, A., 2010. Representative elementary volume analysis of porous media using X-ray computed tomography. *Powder Technol.* 200 (1–2), 69–77. <https://doi.org/10.1016/j.powtec.2010.02.011>.
- Algaazlan, M., Pinetown, K., Grigore, M., Chen, Z., Sarmadivaleh, M., Roshan, H., 2019. Petrophysical assessment of Australian organic-rich shales: Beetaloo, Cooper and Perth basins. *J. Nat. Gas Sci. Eng.* 70, 102952. <https://doi.org/10.1016/j.jngse.2019.102952>.
- Arshadi, M., Zolfaghari, A., Piri, M., Al-Muntasher, G.A., Sayed, M., 2017. The effect of deformation on two-phase flow through proppant-packed fractured shale samples: A micro-scale experimental investigation. *Adv. Water Resour.* 105, 108–131. <https://doi.org/10.1016/j.advwatres.2017.04.022>.
- Asadi, P., Beckingham, L.E., 2021. Integrating Machine/Deep Learning Methods and Filtering Techniques for Reliable Mineral Phase Segmentation of 3D X-ray Computed Tomography Images. *Energies* 14 (15), 4595.
- Chaumette, F., 2004. Image moments: a general and useful set of features for visual servoing. *IEEE Trans. Rob.* 20 (4), 713–723. <https://doi.org/10.1109/TRO.2004.829463>.
- Cheng, G., Guo, W., 2017. Rock images classification by using deep convolution neural network. *J. Phys. Conf. Ser. IOP Publ.* 887, 012089. <https://doi.org/10.1088/1742-6596/887/1/012089>.
- Christe, P., Bernasconi, M., Vontobel, P., Turberg, P., Parriaux, A., 2007. Three-dimensional petrographical investigations on borehole rock samples: a comparison between X-ray computed-and neutron tomography. *Acta Geotech.* 2 (4), 269–279.
- Deng, H., Fitts, J.P., Peters, C.A., 2016. Quantifying fracture geometry with X-ray tomography: Technique of Iterative Local Thresholding (TILT) for 3D image segmentation. *Comput. Geosci.* 20 (1), 231–244.
- Derpanis, K.G., Gryn, J.M., 2005. Three-dimensional nth derivative of Gaussian separable steerable filters, IEEE International Conference on Image Processing 2005. IEEE, pp. III-553.
- Eberly, D., Gardner, R., Morse, B., Pizer, S., Scharlach, C., 1994. Ridges for image analysis. *J. Math. Imaging Vision* 4 (4), 353–373.
- Fonseka, G.M., Murrell, S.A.F., Barnes, P., 1985. Scanning electron microscope and acoustic emission studies of crack development in rocks, International Journal of Rock Mechanics and Mining Sciences & Geomechanics Abstracts. Elsevier 22 (5), 273–289.
- Fornaro, J., Székely, G., Harders, M., 2010. Semi-automatic segmentation of fractured pelvic bones for surgical planning. International symposium on biomedical simulation. Springer 82–89.
- Frangi, A.F., Niessen, W.J., Vincken, K.L., Viergever, M.A., 1998. Multiscale vessel enhancement filtering, International conference on medical image computing and computer-assisted intervention. Springer 130–137.
- Freeman, W.T., Adelson, E.H., 1991. The design and use of steerable filters. *IEEE Trans. Pattern Anal. Mach. Intell.* 13 (9), 891–906.
- Gomila, R., Arancibia, G., Nehler, M., Bracke, R., Morata, D., Cembrano, J., 2021. Quantitative anisotropies of palaeopermeability in a strike-slip fault damage zone: Insights from micro-CT analysis and numerical simulations. *Tectonophysics* 810, 228873. <https://doi.org/10.1016/j.tecto.2021.228873>.
- Gonzalez, R.C., Woods, R.E., 2018. Digital image processing. Pearson.
- He, L., Ren, X., Gao, Q., Zhao, X., Yao, B., Chao, Y., 2017. The connected-component labeling problem: A review of state-of-the-art algorithms. *Pattern Recogn.* 70, 25–43. <https://doi.org/10.1016/j.patcog.2017.04.018>.
- Hsieh, J., 2009. Computed tomography: principles, design, artifacts, and recent advances. SPIE Bellingham, WA.
- Iassonov, P., Gebrenegus, T., Tuller, M., 2009. Segmentation of X-ray computed tomography images of porous materials: A crucial step for characterization and quantitative analysis of pore structures. *Water Resour. Res.* 45 (9), n/a-n/a. <https://doi.org/10.1029/2009WR008087>.
- Ibanez, L., Schroeder, W., Ng, L., Cates, J., 2005. The ITK software guide.
- Johns, R.A., Steude, J.S., Castanier, L.M., Roberts, P.V., 1993. Nondestructive measurements of fracture aperture in crystalline rock cores using X ray computed tomography. *J. Geophys. Res. Solid Earth* 98 (B2), 1889–1900.
- Karimpouli, S., Tahmasebi, P., Ramandi, H.L., 2020a. A review of experimental and numerical modeling of digital coalbed methane: Imaging, segmentation, fracture modeling and permeability prediction. *Int. J. Coal Geol.* 228, 103552. <https://doi.org/10.1016/j.coal.2020.103552>.
- Karimpouli, S., Tahmasebi, P., Saenger, E.H., 2020b. Coal cleat/fracture segmentation using convolutional neural networks. *Nat. Resour. Res.* 29 (3), 1675–1685.
- Karpyn, Z.T., Grader, A.S., Halleck, P.M., 2007. Visualization of fluid occupancy in a rough fracture using micro-tomography. *J. Colloid Interface Sci.* 307 (1), 181–187.
- Katsevich, A., 2002. Theoretically exact filtered backprojection-type inversion algorithm for spiral CT. *SIAM J. Appl. Math.* 62 (6), 2012–2026.
- Keller, A., 1998. High resolution, non-destructive measurement and characterization of fracture apertures. *Int. J. Rock Mech. Min. Sci.* 35 (8), 1037–1050. [https://doi.org/10.1016/S0148-9062\(98\)00164-8](https://doi.org/10.1016/S0148-9062(98)00164-8).
- Ketcham, R.A., 2005. Computational methods for quantitative analysis of three-dimensional features in geological specimens. *Geosphere* 1 (1), 32–41.
- Ketcham, R.A., Carlson, W.D., 2001. Acquisition, optimization and interpretation of X-ray computed tomographic imagery: applications to the geosciences. *Comput. Geosci.* 27 (4), 381–400. [https://doi.org/10.1016/s0098-3004\(00\)00116-3](https://doi.org/10.1016/s0098-3004(00)00116-3).
- Ketcham, R.A., Slottke, D.T., Sharp, J.M., 2010. Three-dimensional measurement of fractures in heterogeneous materials using high-resolution X-ray computed tomography. *Geosphere* 6 (5), 499–514.
- Li, B.O., Mo, Y., Zou, L., Liu, R., Cvetkovic, V., 2020. Influence of surface roughness on fluid flow and solute transport through 3D crossed rock fractures. *J. Hydrol.* 582, 124284. <https://doi.org/10.1016/j.jhydrol.2019.124284>.
- Li, Y., Shi, D., Bu, F., 2019. Automatic Recognition of Rock Images Based on Convolutional Neural Network and Discrete Cosine Transform. *Traitement du Signal* 36 (5), 463–469.
- Liang, Y., 2016. Rock fracture skeleton tracing by image processing and quantitative analysis by geometry features. *J. Geophys. Eng.* 13 (3), 273–284.
- Lindqvist, P.-A., Lai, H.H., Alm, O., 1984. Indentation fracture development in rock continuously observed with a scanning electron microscope, International Journal of Rock Mechanics and Mining Sciences & Geomechanics Abstracts. Elsevier 21 (4), 165–182.
- Lopez, A.M., Lumbrieras, F., Serrat, J., Villanueva, J.J., 1999. Evaluation of methods for ridge and valley detection. *IEEE Trans. Pattern Anal. Mach. Intell.* 21 (4), 327–335.
- Lv, A., Ramandi, H.L., Masoumi, H., Saadatfar, M., Regenauer-Lieb, K., Roshan, H., 2019. Analytical and experimental investigation of pore pressure induced strain softening around boreholes. *Int. J. Rock Mech. Min. Sci.* 113, 1–10. <https://doi.org/10.1016/j.ijrmms.2018.11.001>.
- Mazumder, S., Wolf, K.H.A.A., Elewaut, K., Ephraim, R., 2006. Application of X-ray computed tomography for analyzing cleat spacing and cleat aperture in coal samples. *Int. J. Coal Geol.* 68 (3–4), 205–222. <https://doi.org/10.1016/j.coal.2006.02.005>.
- Pruess, K., Tsang, Y.W., 1990. On two-phase relative permeability and capillary pressure of rough-walled rock fractures. *Water Resour. Res.* 26 (9), 1915–1926.
- Qajar, J., Francois, N., Arns, C.H., 2012. Micro-tomographic characterization of dissolution-induced local porosity changes including fines migration in carbonate rock. *SPE J.* 18 (03), 545–562. <https://doi.org/10.2118/153216-PA>.
- Qi, C., Wang, X., Wang, W., Liu, J., Tu, J., Liu, K., 2018. Three-dimensional characterization of micro-fractures in shale reservoir rocks. *Petroleum Res.* 3 (3), 259–268.
- Ramandi, H.L., Armstrong, R.T., Mostaghimi, P., 2016a. Micro-CT image calibration to improve fracture aperture measurement. *Case Stud. Nondestr. Test. Eval.* 6, 4–13.

- Ramandi, H.L., Armstrong, R.T., Mostaghimi, P., Saadatfar, M., Pinczewski, W.V., 2015. X-Ray Micro-Computed Tomography Imaging for Coal Characterization, SPE Asia Pacific Unconventional Resources Conference and Exhibition. Society of Petroleum Engineers. DOI:<https://doi.org/10.2118/177017-MS>.
- Ramandi, H.L., Mostaghimi, P., Armstrong, R.T., 2017. Digital rock analysis for accurate prediction of fractured media permeability. *J. Hydrol.* 554 (Supplement C), 817–826. <https://doi.org/10.1016/j.jhydrol.2016.08.029>.
- Ramandi, H.L., Mostaghimi, P., Armstrong, R.T., Saadatfar, M., Pinczewski, W.V., 2016b. Porosity and permeability characterization of coal: a micro-computed tomography study. *Int. J. Coal Geol.* 154–155, 57–68. <https://doi.org/10.1016/j.coal.2015.10.001>.
- Ramandi, L.H., Chen, H., Crosky, A., Saydam, S., 2018. Interactions of stress corrosion cracks in cold drawn pearlitic steel wires: An X-ray micro-computed tomography study. *Corros. Sci.* 145, 170–179. <https://doi.org/10.1016/j.corsci.2018.09.009>.
- Rocha, L., Velho, L., Carvalho, P.C.P., 2002. Image moments-based structuring and tracking of objects, Proceedings. In: XV Brazilian Symposium on Computer Graphics and Image Processing, pp. 99–105. <https://doi.org/10.1109/SIBGRA.2002.1167130>.
- Roshan, H., Chen, X., Pirzada, M.A., Regenauer-Lieb, K., 2019. Permeability measurements during triaxial and direct shear loading using a novel X-ray transparent apparatus: fractured shale examples from Beetaloo basin, Australia. *NDT E Int.* 107, 102129. <https://doi.org/10.1016/j.ndteint.2019.102129>.
- Schlüter, S., Sheppard, A., Brown, K., Wildenschild, D., 2014. Image processing of multiphase images obtained via X-ray micromotography: A review. *Water Resour. Res.* 50 (4), 3615–3639. <https://doi.org/10.1002/2014WR015256>.
- Schneider, C.A., Rasband, W.S., Eliceiri, K.W., 2012. NIH Image to ImageJ: 25 years of image analysis. *Nat. Methods* 9 (7), 671–675.
- Serati, M., Bahaaddini, M., Roshan, H., Zhang, T.T., Bryant, N., 2021. On assessing the tensile cracking pattern in brittle rocks and solids. *Bull. Eng. Geol. Environ.* 80 (7), 5867–5879.
- Sezgin, M., Sankur, B., 2004. Survey over image thresholding techniques and quantitative performance evaluation. *J. Electron. Imaging* 13 (1), 146–166.
- Sheppard, A., Latham, S., Middleton, J., Kingston, A., Myers, G., Varslot, T., Fogden, A., Sawkins, T., Cruikshank, R., Saadatfar, M., Francois, N., Arns, C., Senden, T., 2014. Techniques in helical scanning, dynamic imaging and image segmentation for improved quantitative analysis with X-ray micro-CT. *Nucl. Instrum. Methods Phys. Res., Sect. B* 324, 49–56. <https://doi.org/10.1016/j.nimb.2013.08.072>.
- Sheppard, A.P., Sok, R.M., Averdunk, H., 2004. Techniques for image enhancement and segmentation of tomographic images of porous materials. *Physica A* 339 (1–2), 145–151. <https://doi.org/10.1016/j.physa.2004.03.057>.
- Siddiqui, M.A.Q., Salvemini, F., Ramandi, H.L., Fitzgerald, P., Roshan, H., 2021. Configurational diffusion transport of water and oil in dual continuum shales. *Sci. Rep.* 11 (1), 2152. <https://doi.org/10.1038/s41598-021-81004-1>.
- Smith, O.K., 1961. Eigenvalues of a symmetric 3×3 matrix. *Commun. ACM* 4 (4), 168. <https://doi.org/10.1145/355578.366316>.
- Soulaine, C., Gjetvaj, F., Garing, C., Roman, S., Russian, A., Gouze, P., Tchelepi, H.A., 2016. The impact of sub-resolution porosity of X-ray microtomography images on the permeability. *Transp. Porous Media* 113 (1), 227–243.
- Stathis, P., Kavallieratou, E., Papamarkos, N., 2008. An Evaluation Technique for Binarization Algorithms. *J. UCS* 14 (18), 3011–3030.
- Toriwaki, J., Yoshida, H. (Eds.), 2009. *Fundamentals of Three-Dimensional Digital Image Processing*. Springer London, London.
- Van der Walt, S. et al., 2014. scikit-image: image processing in Python. *PeerJ* 2 (2014), e453. arXiv preprint arXiv:1407.6245.
- Van Geet, M., Swennen, R., David, P., 2001. Quantitative coal characterisation by means of microfocus X-ray computer tomography, colour image analysis and back-scattered scanning electron microscopy. *Int. J. Coal Geol.* 46 (1), 11–25. [https://doi.org/10.1016/S0166-5162\(01\)00006-4](https://doi.org/10.1016/S0166-5162(01)00006-4).
- Vandersteen, K., Busselen, B., Van Den Abeele, K., Carmeliet, J., 2003. Quantitative characterization of fracture apertures using microfocus computed tomography. *Geol. Soc. London Special Publ.* 215 (1), 61–68.
- Varslot, T., Kingston, A., Myers, G., Sheppard, A., 2012. Considerations for high-magnification high-cone-angle helical micro-CT, *Developments in X-Ray Tomography VIII*. International Society for Optics and Photonics, p. 850614.
- Verhelst, F., Vervoort, A., BOSSCHER, P.D., Marchal, G., 1995. X-ray computerized tomography: determination of heterogeneities in rock samples, 8th ISRM Congress.
- Voorn, M., Exner, U., Rath, A., 2013. Multiscale Hessian fracture filtering for the enhancement and segmentation of narrow fractures in 3D image data. *Comput. Geosci.* 57, 44–53.
- Wang, Y., Teng, Q., He, X., Feng, J., Zhang, T., 2019. CT-image of rock samples super resolution using 3D convolutional neural network. *Comput. Geosci.* 133, 104314. <https://doi.org/10.1016/j.cageo.2019.104314>.
- Wang, Z., Zhou, C., Wang, F., Li, C., Xie, H., 2021. Channeling flow and anomalous transport due to the complex void structure of rock fractures. *J. Hydrol.* 601, 126624. <https://doi.org/10.1016/j.jhydrol.2021.126624>.
- Yang, X., et al., 2019. Quantifying 2D and 3D Fracture Leakage Pathways Observed in Wellbore Cement after Uniaxial Compressive Loading. Society of Petroleum Engineers, SPE Thermal Well Integrity and Design Symposium.
- Zhang, Z.X., Kou, S.Q., Yu, J., Yu, Y., Jiang, L.G., Lindqvist, P.-A., 1999. Effects of loading rate on rock fracture. *Int. J. Rock Mech. Min. Sci.* 36 (5), 597–611. [https://doi.org/10.1016/S0148-9062\(99\)00031-5](https://doi.org/10.1016/S0148-9062(99)00031-5).
- Zhao, H., Luo, N., Illman, W.A., 2021. The importance of fracture geometry and matrix data on transient hydraulic tomography in fractured rocks: Analyses of synthetic and laboratory rock block experiments. *J. Hydrol.* 601, 126700. <https://doi.org/10.1016/j.jhydrol.2021.126700>.
- Zhou, S., Yan, G., Xue, H., Guo, W., Li, X., 2016. 2D and 3D nanopore characterization of gas shale in Longmaxi formation based on FIB-SEM. *Mar. Pet. Geol.* 73, 174–180. <https://doi.org/10.1016/j.marpetgeo.2016.02.033>.